JPhys Energy

PAPER • OPEN ACCESS

Electronic scattering in half-Heusler thermoelectrics from resistivity data

To cite this article: Robert J Quinn *et al* 2022 *J. Phys. Energy* **4** 024005

View the article online for updates and enhancements.

You may also like

- *(Invited)* Electric Dipole-Electric Dipole Non-Radiative Energy Transfer Mediated By Surface Plasmons on a Metal Surface
  Kailash C. Mishra and John Collins
- Extraordinary Hall effect in $Ba_{1-x}Sr_xRuO_3$
  Y Kobayashi, M Iwata, T Kaneko et al.
- The quark strange star in the enlarged Nambu-Jona-Lasinio model
  Ryszard Manka, Ilona Bednarek and Grzegorz Przybyla

This content was downloaded from IP address 51.9.215.203 on 12/07/2023 at 15:04

Journal of Physics: Energy

OPEN ACCESS

RECEIVED
9 December 2021

REVISED
7 March 2022

ACCEPTED FOR PUBLICATION
18 March 2022

PUBLISHED
7 April 2022

Original content from this work may be used under the terms of the Creative Commons Attribution 4.0 licence.

Any further distribution of this work must maintain attribution to the author(s) and the title of the work, journal citation and DOI.

PAPER

Electronic scattering in half-Heusler thermoelectrics from resistivity data

Robert J Quinn[1,*], **Gavin B G Stenning**[2] **and Jan-Willem G Bos**[1,*]

[1] Institute of Chemical Sciences and Centre for Energy Storage and Recovery, School of Engineering and Physical Sciences, Heriot-Watt University, Edinburgh EH14 4AS, United Kingdom
[2] Materials Characterisation Laboratory, ISIS Neutron and Muon Source, Rutherford Appleton Laboratory, Didcot, Oxfordshire OX11 0QX, United Kingdom
[*] Authors to whom any correspondence should be addressed.

E-mail: r.quinn@hw.ac.uk **and** j.w.g.bos@hw.ac.uk

Keywords: Heusler alloys, thermoelectric properties, deformation potential, electrical resistivity

Abstract

A key part of optimising thermoelectric materials is understanding the electronic scattering mechanism. For half-Heusler (HH) thermoelectrics, the dominant mechanisms are acoustic phonon scattering in pure systems and alloy scattering in highly alloyed systems. In this report, the significance of the residual resistivity ρ_0 is highlighted. Large ρ_0 values can lead to misidentification of the dominant scattering mechanism when only high-temperature $\rho(T)$ data is available. A straightforward approach to analyse $\rho(T)$ is proposed and applied to a range of HH systems. This reveals large levels of structural disorder in $X_{IV}NiSn$, whilst $X_{V}FeSb$ has the strongest coupling with acoustic phonons. The electronic scattering mechanism depends sensitively on composition, with acoustic ($\rho \sim T^{1.5}$), metallic ($\sim T^1$) and alloy ($\sim T^{0.5}$) scattering observed within the main HH families. With the aid of velocity of sound, band mass and carrier concentration data, the deformation potential can be obtained, enabling quantification of the interaction between phonons and carriers, from fits to resistivity data. This work provides a route for the analysis of experimental $\rho(T)$ data that can be applied to a range of thermoelectric materials.

1. Introduction

Semiconducting half-Heusler (HH) phases are promising candidates for thermoelectric applications, boasting high power factors, mechanical stability and high abundance constituent elements [1–6]. Accurate determination of the electronic scattering mechanism is important because it can provide guidance on optimisation, by promoting phonon scattering, while charge carrier scattering is suppressed [7–9]. At present, the dominant scattering contributions to the mobility μ in HH compounds are considered to be acoustic phonon scattering (APS) and alloy scattering (AS) [10–12]. These have different temperature dependences, $\mu \sim T^{-1.5}$ for APS and $\sim T^{-0.5}$ for AS in the non-degenerate limit [13–15]. In the metallic limit APS is expected to dominate, with a $\sim T^1$ temperature dependence [14], as demonstrated by the Bloch–Grüneisen model [16]. For extrinsically doped compositions, under the assumption that the carrier concentration (n_H) is temperature independent, the electrical conductivity ($\sigma = n_H e \mu_H$) or resistivity ($\rho = 1/\sigma$) are directly proportional to μ_H and can be used to establish the dominant carrier scattering mechanism. Here, n_H and μ_H are the carrier concentration and mobility from Hall measurements, and e is the electron charge.

Under the above assumptions of scattering behaviour, a number of methods have been employed to understand $\rho(T)$, $\mu(T)$ and the underlying scattering. The simplest approach is to use a linear fit of either $\rho(T)$ or $\mu(T)$ on logarithmic axes in order to determine the temperature exponent. Another approach uses band modelling to fit the n_H dependence of μ_H at fixed temperature, with Matthiessen's rule used to balance contributions of APS and AS, although this is difficult as both have identical n_H dependence [14, 15, 17]. Direct fitting of $\rho(T)$ is most commonly seen in low-temperature data using the Bloch–Grüneisen model in

© 2022 The Author(s). Published by IOP Publishing Ltd

highly metallic samples [18, 19], with APS as the dominant scattering mechanism. Some modelling has been done to account for the effects of grain boundary scattering close to room temperature [20–22].

In this paper, the $\rho(T)$ data of a range of degenerately doped HH materials is examined in order to examine scattering. This is convenient given the large volume of $\rho(T)$ data available relative to $\mu_H(T)$ data. The article starts with an overview of the $\rho(T)$ behaviour expected in metals and degenerate semiconductors and of the typical approach taken in the literature for analysing the temperature dependence. A fitting model incorporating a residual resistivity ρ_0, either APS or AS scattering and intrinsic carrier excitations is applied to a range of HH systems, first validating it for compositions where low-temperature $\rho(T)$ data is available and then applying it to a broad range of high-temperature data sets. Finally, deformation potential values are extracted from the fits to $\rho(T)$ data for the samples that show semiconductor APS behaviour, enabling a straightforward estimate of the strength of the coupling of charge carriers and acoustic phonons.

2. Carrier scattering in metals and degenerate semiconductors

For metals, $\rho(T)$ is linear at high temperatures and characterised by a limiting non-zero ρ_0 at 0 K. This is described by the Bloch–Grüneisen model [16]:

$$\rho(T) = \rho_0 + A\left(\frac{T}{\theta_D}\right)^i \int_0^{\frac{\theta_D}{T}} \frac{x^i}{(e^x - 1)(1 - e^{-x})} dx \tag{1}$$

where i is used to describe the dominant scattering mechanism, with a T^i temperature dependence observable at low temperatures ($i = 5$ for APS, $i = 2$ for electron–electron scattering), before scaling linearly at higher temperatures ($\sim T^1$) with an increase in phonon population. The residual resistivity ρ_0 exists due to defects present in the system (e.g. point defects, dislocations, and grain boundary effects in polycrystalline samples).

In semiconductors, three carrier scattering mechanisms are typically considered to be relevant. Ionised impurity scattering (IIS) due to interaction with charged impurities dominates at low carrier concentrations and follows $\rho \sim T^{-1.5}$ [14, 15]. This scattering mechanism is typically not relevant to optimally doped HH materials as these have large carrier concentrations, which screen the ionised impurities [15]. The other two mechanisms have already been introduced, APS varies as $\rho \sim T^{1.5}$, as the phonon population increases with temperature [13–15]. Finally AS is expected to have a $\rho \sim T^{0.5}$ temperature dependence [14, 15], and should scale with $x(1 - x)$ where x is the alloying fraction on a site [23]. In the heavily doped degenerate semiconducting limit, both IIS and AS are considered temperature independent and APS follows a $\sim T^1$ dependence, in line with the Bloch–Grüneisen model [14, 15].

At present, the temperature dependence of $\rho(T)$ (or $\sigma(T)$, $\mu_H(T)$) is typically treated by analysing the slope of a straight line on a logarithmic plot of the data ($\log \rho = i \log T$). However, this assumes that there is a negligible ρ_0, which may not be the case. As illustrated below, the presence of a substantial ρ_0 will alter the apparent temperature dependence at high temperatures. For HH systems when trying to decide between APS and AS, this can be a crucial factor to consider. The solution is to explicitly incorporate ρ_0, following the Bloch–Grüneisen model for metals:

$$\rho(T) = \rho_0 + BT^{1.5}. \tag{2}$$

In this model, ρ_0 and B are related to temperature independent electronic scattering and the strength of APS, respectively. As for the Bloch–Grüneisen model, ρ_0 is linked to imperfections in the material and can be taken to be a measure of disorder. Dividing ρ_0/B gives a measure of the relative impact of structural disorder and APS on the electronic carrier scattering. If there is a substantial ρ_0 contribution, the increase in $\rho(T)$ will appear reduced from a $T^{1.5}$ dependence when plotted on a log–log plot.

Figure 1 shows examples of equation (2) with increasing ρ_0 and fixed B. Panel (a) shows data over the full 0 K–1000 K range and the $T^{1.5}$ temperature dependence is clear at high temperatures, with $\rho(T)$ simply shifted upwards by ρ_0. Panel (b) shows a logarithmic plot of the 300 K–1000 K data. Using the slope to estimate i leads to an increasing underestimate of the true temperature dependence. For example, the sample with the largest ρ_0 is estimated to have $i \sim 0.5$, but in fact has $i = 1.5$ with a large ρ_0.

At high temperatures, many materials experience a decrease in $\rho(T)$ due to the thermal excitation of intrinsic carriers. In this case there are two parallel conduction channels and equation (2) can be modified to include an Arrhenius term:

$$\rho(T)^{-1} = \left(\rho_0 + BT^{1.5}\right)^{-1} + \left(Ae^{\frac{-E_g}{2k_B T}}\right)^{-1}. \tag{3}$$

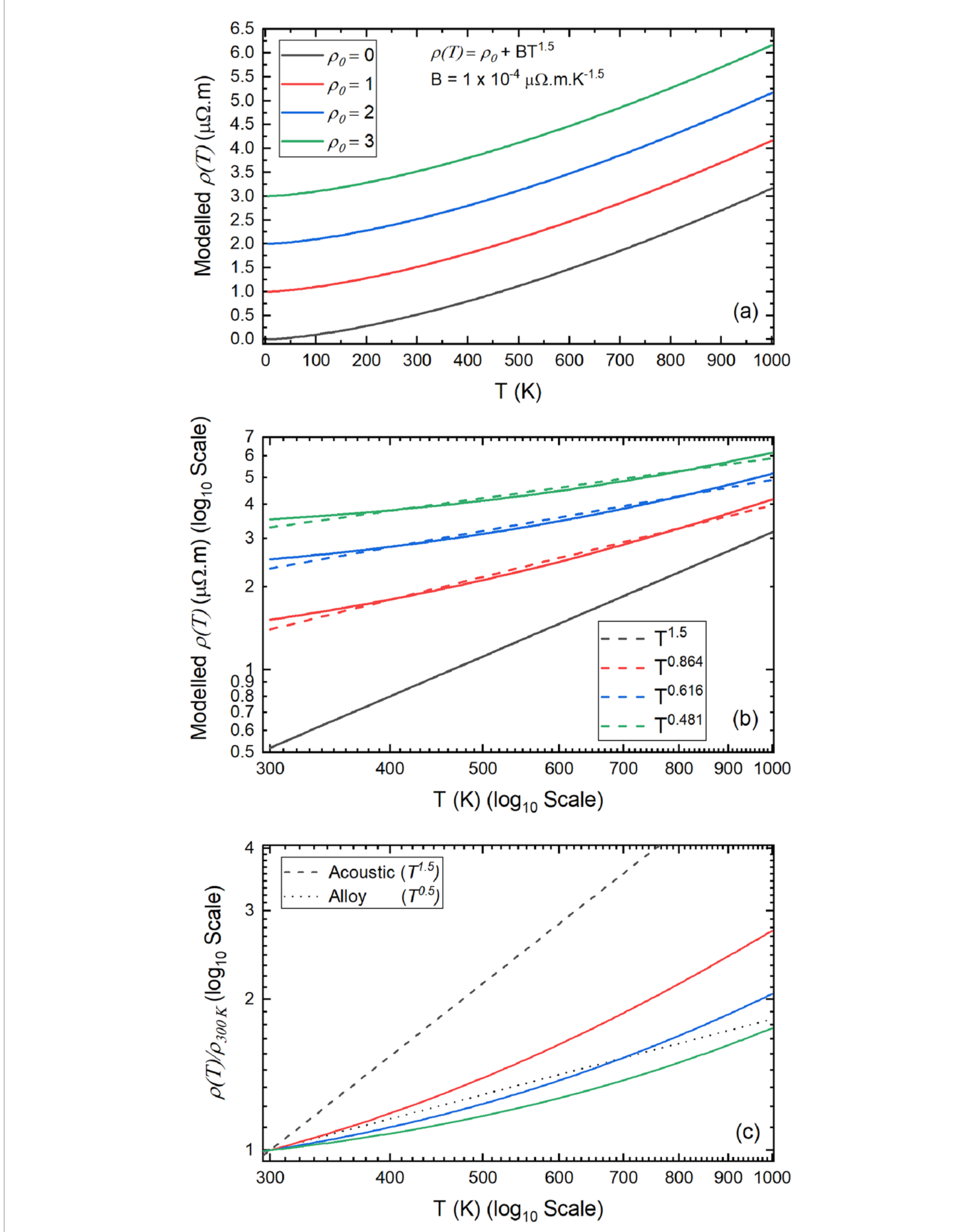

Figure 1. Modelled electrical resistivities using fixed APS ($B = 1 \times 10^{-4}$ $\mu\Omega$ m $K^{-1.5}$) and increasing residual resistivity ($\rho_0 = 0 \rightarrow 4$ $\mu\Omega$ m). Panel (a) shows $\rho(T)$ over a wide temperature range from 2 K to 1000 K. Panel (b) shows the same data between 300 K and 1000 K on logarithmic scales and the linear fits (dashed lines) commonly used to assign the carrier scattering mechanism. Panel (c) plots $\rho(T)$ normalized with respect to $\rho_{300\,\mathrm{K}}$ and includes the predicted pure APS $T^{1.5}$ (dashed) and AS $T^{0.5}$ temperature dependences. The upwards curvature in plot (c) shows that $\rho(T)$ approaches $T^{1.5}$ as $T \rightarrow \infty$ and that $\rho(T)$ is increasingly limited by APS.

To check how an alloying model compares, the following closely related equation can be used:

$$\rho(T)^{-1} = \left(\rho_0 + CT^{0.5}\right)^{-1} + \left(Ae^{\frac{-E_g}{2k_B T}}\right)^{-1}. \tag{4}$$

The final panel of figure 1 shows 300 K normalised data, $\rho(T)/\rho_{300\,\mathrm{K}}$, on a logarithmic plot. This normalisation was chosen to have a standard method of presenting data that focusses on temperature dependence but is not obscured by differences in magnitude. As can be seen in panel (c), the pure APS and

AS trends (i.e. $\rho_0 = 0$) remain linear with logarithmic axes. As ρ_0 is increased, the line is pushed further below the ideal APS dependence but is never linear on the logarithmic plot. It is this absence of a linear regime that signals the presence of a significant ρ_0 contribution. This is true whether or not the scattering mechanism turns out to be APS or AS: the absence of a linear domain implies a substantial ρ_0. At elevated temperatures, the upwards curvature is due to the slope approaching $T^{1.5}$ (or $T^{0.5}$ for AS) as $T \to \infty$. In situations with moderate ρ_0 (or sufficiently high temperature data) it is therefore possible to inspect for a slope $i > 0.5$ at high temperatures, which would indicate APS. A final possibility is a transition from AS to APS with increasing temperature, which is not unrealistic given the stronger temperature dependence of APS. In a pure dual mechanism system, two linear regions ($T^{0.5}$ and $T^{1.5}$) are expected, separated by a curved region as dominance shifts from AS to APS. A significant ρ_0 would lead to curvature in both AS and APS domains. In this case equation (2) can be extended to include a $CT^{0.5}$ term, which should be adequate to describe such a transition in a degenerate system.

In the above models, it is assumed that either APS or AS is present, but not at the same time. In the analysis below, it was never necessary to include both scattering mechanisms in order to achieve an adequate fit to the data and it was considered that including too many fitting parameters would reduce the overall significance of the values obtained. In principle, the two scattering mechanisms could be used in parallel by appropriately weighting $BT^{1.5}$ and $CT^{0.5}$ terms using Matthiessen's rule.

3. Validation of the model using temperature resistivity data

Although not commonly collected, low-temperature $\rho(T)$ data is available for the main HH families. In case of $ZrNiSn_{1-x}Sb_x$, both single crystal and polycrystalline data has recently been reported [11]. The samples digitised for this manuscript have 7.3×10^{19} cm^{-3} $< n_H < 2.6 \times 10^{21}$ cm^{-3}, which covers the typical range for optimal thermoelectric performance (figure 2). These samples are all degenerate semiconductors with $\rho(T)$ described well by equation (2), indicating APS with a substantial ρ_0 contribution (table 1). Figure 2(c) plots ρ_0/B, from which two key observations can be made. Firstly, ρ_0/B decreases with increasing doping, consistent with stronger APS at higher n_H [12]. Secondly, ρ_0/B is larger for polycrystalline samples (at a given n_H), consistent with the larger intrinsic disorder compared to single crystals.

No other single crystal data is available, but a number of reports contain low- and high-temperature data on polycrystalline samples. $\rho(T)$ for selected members of the n-type $X_{IV}NiSn$, $X_{V0.8}CoSb$ and p-type X_VFeSb (X_{IV} = Ti, Zr, Hf; X_V = V, Nb, Ta) families are shown in figure 3. The $TiNiCu_{0.025}Sn$ sample in panel (a) shows good agreement with equation (2) up to 700 K, above which intrinsic carriers begin to contribute. The $X_{IV}NiSn$ samples in panel (b) show much better agreement with the Bloch–Grüneisen model, as noted in the original papers [18, 19], rather than equation (2) and hence have $\rho \sim T$ at high-temperature. The reported n_H values (8–10 $\times 10^{20}$ cm^{-3}) are comparable to the most highly doped $ZrNiSn_{1-x}Sb_x$ samples in figure 2, which follow standard semiconductor APS. The change from $T^{1.5}$ to T^1 is therefore not only associated with carrier concentration. The consistent feature amongst all $X_{IV}NiSn$ samples, including those discussed below is that they have a very significant ρ_0, making up at around 50% of the total resistivity at 800 K.

Figure 3(c) shows data for $X_{V0.8}CoSb$ (X_V = V, Nb) samples, which have a linear temperature dependence in keeping with Bloch–Grüneisen behaviour. This is consistent with the very large metallic n_H, approaching 1×10^{22} cm^{-3} for these samples [24, 25]. One immediate comparison that can made with respect to the $X_{IV}NiSn$ family is that relative to ρ_0, the temperature dependence of $\rho(T)$ is much stronger. Both systems are expected to be highly disordered: $X_{IV}NiSn$ is famous for high concentrations of interstitial Ni known to suppress μ_H [26], while $X_{V0.8}CoSb$ is famous for a partially vacant X_V-site [24, 25]. Both might be expected to lead to large ρ_0 values, but the strong temperature dependence shows that the impact is less significant in the $X_{V0.8}CoSb$ family.

The final set of data presented in figure 3(d) is for $Nb_{0.8}Ti_{0.2}FeSb$ with $n_H \sim 2.2 \times 10^{21}$ cm^{-3} [27]. $\rho(T)$ is in agreement with equation (2) above 300 K, signalling the presence of dominant APS. The increase in $\rho(T)$ is large compared to ρ_0, suggesting that residual disorder is less important than coupling with acoustic phonons. Despite the strong temperature dependence, the magnitude of ρ_0 is comparable to the other systems: e.g. $\rho_0 \sim 0.8$ $\mu\Omega$ m for $Nb_{0.8}Ti_{0.2}FeSb$ and to $\rho_0 \sim 0.7$ $\mu\Omega$ m for $ZrNiSn_{1-x}Sb_x$ with similar n_H. This indicates that the strength of the coupling with acoustic phonons is very different in the $X_{IV}NiSn$ and X_VFeSb families. Below 300 K, $\rho(T)$ has a T^2 temperature dependence (figure 3(d)), which has been attributed to magnetic effects [27].

From the HH samples examined, it is clear that ρ_0 is a significant fraction of the total temperature dependence of $\rho(T)$ for the $X_{IV}NiSn$ family. By contrast, the $Nb_{0.8}Ti_{0.2}FeSb$ sample shows a much stronger temperature dependence and has a much lower relative impact of ρ_0 (only ∼10% of $\rho_{800\,K}$ compared to ∼50% for $TiNiCu_{0.025}Sn$). This strong temperature dependence is significant for the thermoelectric properties, with the power factor, S^2/ρ typically decreasing with temperature in the X_VFeSb system, whereas

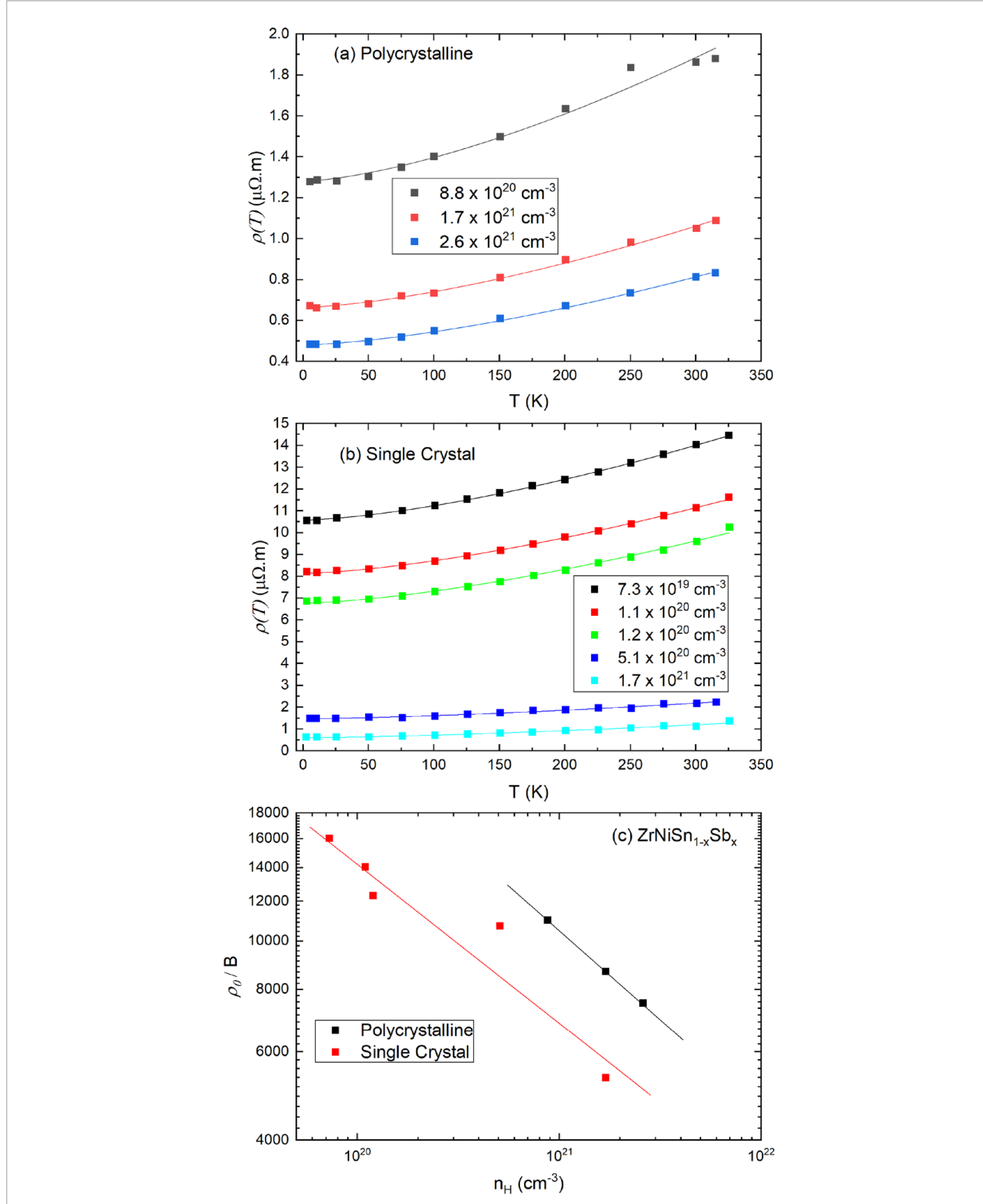

Figure 2. Digitised 4 K–300 K literature electrical resistivity data for $ZrNiSn_{1-x}Sb_x$ samples [11]. Panels (a) and (b) show polycrystalline and single crystal samples. Solid lines are fits to the APS model (equation (2)). Panel (c) shows the expected decrease of ρ_0/B with carrier concentration, as the relative strength of APS increases (table 1).

they increase in the $X_{IV}NiSn$ family [21, 28, 29]. The samples in figure 3 either have a T^1 or $T^{1.5}$ dependence of $\rho(T)$. Both are consistent with APS, with the smaller temperature dependence (Bloch–Grüneisen) usually linked to highly degenerate systems. There is no clear crossover between these different behaviours based on doping level. This demonstrates that carrier scattering depends on subtle details of the chemical composition and can show considerable variation within each family.

4. Analysis of high-temperature resistivity data for a range of half-Heusler (HH) systems

High temperature normalised $\rho(T)/\rho_{300\,K}$ data for selected compositions from the main HH families are plotted in figure 4. Normalisation of the data allows for the temperature dependence to be examined

Table 1. Overview of parameters used to fit electrical resistivity data for a range of HH families. The ρ_0, B and A parameters are defined in the text[a]. Hall carrier concentrations (n_H) and band masses ($m_b{}^*$) were obtained from the source publication or estimated from the literature. An overview of $m_b{}^*$ and longitudinal velocities of sound (v_l) can be found in [2]. The deformation potential (E_{def}) was obtained using equation (8).

		ρ_0 ($\mu\Omega$ m)	B ($\times 10^{-4}$ $\mu\Omega$ m K$^{-1.5}$)	A ($\mu\Omega$ m)	ρ_0/B (K$^{1.5}$)	n_H ($\times 10^{20}$ cm^{-3})	$m_b{}^*$ (m_e)	$m_{DoS}{}^*$ (m_e)	E_{def} (eV)
$Ti_{1-x}Ta_xNi_{0.92}Sn$ [30]	$x = 0.01$	7.95	4.09	0.6717	19 453	2.45	1.35 (2.16)[b]	4.5	7.1 (3.9)
	$x = 0.02$	4.32	3.23	0.577 72	13 382	4.63	1.35 (2.16)	4.5	8.5 (4.7)
	$x = 0.025$	2.36	2.59	0.283 91	9101	6.03	1.35 (2.16)	4.5	8.6 (4.8)
	$x = 0.03$	1.81	2.34	0.1934	7731	7.19	1.35 (2.16)	4.5	8.9 (5.0)
	$x = 0.05$	1.35	1.64	0	8225	10.6	1.35 (2.16)	4.5	8.9 (5.0)
$TiNiSn_{0.99-x}Sb_x$ [31]	$x = 0.02$	2.43	2.23	0.6728	10 891	5.3	1.35	2.8	7.6
	$x = 0.055$	1.21	1.34	0.160 79	8984	10.0	1.35	2.8	7.6
$ZrCoBi_{1-x}Sn_x$ [34, 40]	$x = 0.05$	8.74	10.03	0.093 42	8710	7.36	2.8	13	7.8
	$x = 0.1$	5.60	5.85	0.2218	9560	14.7	2.8	13	8.3
	$x = 0.15$	4.13	4.50	0.233 79	9164	22.1	2.8	13	8.9
	$x = 0.2$	4.22	3.60	0.227 81	11 739	27.1	2.8	13	8.7
$Nb_{1-x}Zr_xFeSb$ [28]	$x = 0.08$	0.45	4.26	0	1064	12.1	1.73	6.9	12.9
	$x = 0.10$	0.52	3.29	0	1578	14.0	1.73	6.9	12.1
	$x = 0.14$	0.61	2.78	0.010 49	2177	19.5	1.73	6.9	13.0
$ZrNiSn_{1-x}Sb_x$ (SC) [11]	—	10.57	6.60	0	16 017	0.73	1.4	3.0	5.0
	—	8.13	5.79	0	14 030	1.10	1.4	3.0	5.7
	—	6.77	5.50	0	12 310	1.20	1.4	3.0	5.8
	—	1.47	1.37	0	10 706	5.10	1.4	3.0	5.8
	—	0.60	1.13	0	5323	17.0	1.4	3.0	8.8
$ZrNiSn_{1-x}Sb_x$ (PC) [11]	—	1.28	1.16	0	10 989	8.80	1.4	3.0	6.8
	—	0.66	0.76	0	8682	17.0	1.4	3.0	7.3
	—	0.48	0.64	0	7507	26.0	1.4	3.0	7.9
$Ta_{1-x}Ti_xFeSb$ [41]	$x = 0.06$	2.10	4.86	0	4329	9.80	2.25	9.0	9.6
	$x = 0.08$	1.04	4.45	0	2348	13.0	2.25	9.0	10.4
	$x = 0.12$	0.45	3.67	0	1225	17.0	2.25	9.0	10.8
	$x = 0.16$	0.72	3.13	0.0436	2307	19.0	2.25	9.0	10.5

(Continued.)

Table 1. (Continued.)

		ρ_0 ($\mu\Omega$ m)	B ($\times10^{-4}$ $\mu\Omega$ m $K^{-1.5}$)	A ($\mu\Omega$ m)	ρ_0/B ($K^{1.5}$)	n_H ($\times10^{20}$ cm^{-3})	m_b^* (m_e)	m_{DoS}^* (m_e)	E_{def} (eV)
$(Nb_{1-x}Ta_x)_{0.8}Ti_{0.2}FeSb$ [42]	$x = 0.24$	0.41	2.15	0.011 46	1910	26.8	1.73	6.9	12.5
	$x = 0.32$	0.24	2.57	0.072 42	921	25.7	1.73	6.9	13.5
	$x = 0.36$	0.16	2.88	0.141 68	559	25.2	1.73	6.9	14.2
$Hf_{0.6}Zr_{0.4}NiSn_{0.99}Sb_{0.01}$ $+x$Wt% W [43]	$x = 0$	7.47	1.83	0.430 68	40 710	1.85	1.35	2.8	4.0
	$x = 2$	7.17	1.49	0.424 26	48 066	2.08	1.35	2.8	3.9
	$x = 5$	5.99	1.26	0.449 96	47 737	2.79	1.35	2.8	4.1
$(Zr_{1-x}Hf_x)_{0.88}Nb_{0.12}CoSb$ [8]	$x = 1$	6.45	2.77	0.014 06	23 257	16.2	3.12	6.5	5.4
	$x = 0.6$	5.51	3.22	0.046 46	17 127	16.3	3.12	6.5	5.9
	$x = 0.3$	6.31	3.30	0.046 24	19 104	15.0	3.12	6.5	5.8
$Nb_{0.8}Ti_{0.2}FeSb$ [27]	—	0.26	2.54	0.057 11	1023	23.0	1.73	6.9	13.4
$TiNiCu_{0.025}Sn$	—	3.98	1.98	0.144 47	20 101	—	—	—	—

[a] A bandgap, $E_g = 0.5$ eV was used for samples with intrinsic carrier excitations.
[b] Calculations use different m_b^*, because it is not established if total degeneracy $N_v = 6$ or $N_v = 3$, with $m^*_{DoS} = N_v^{2/3} m_b^* = 4.5\ m_e$.[2] $N_v = 6$ leads to better agreement of m_b^* and hence E_{def} with the other $X_{IV}NiSn$ phases.

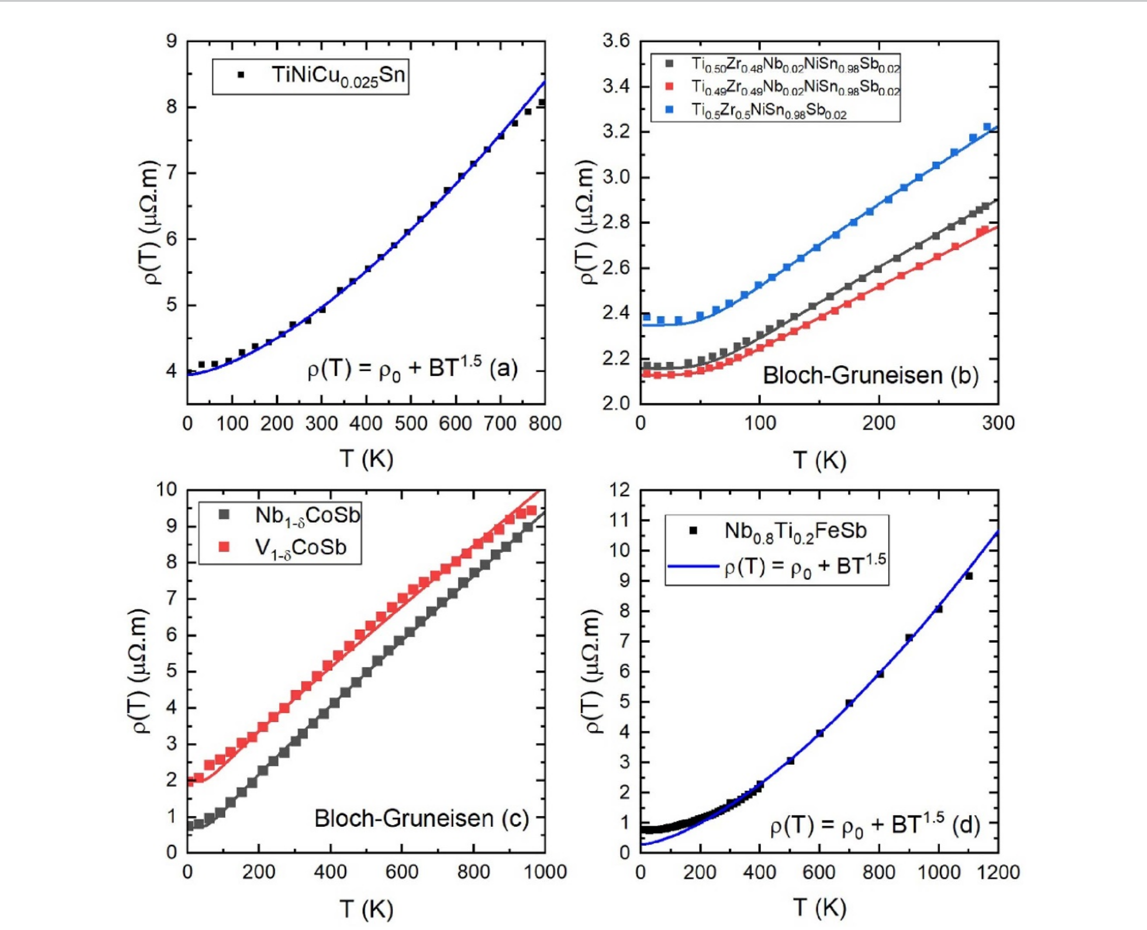

Figure 3. Fits to electrical resistivity ($\rho(T)$) data using either APS (equation (2)) or metallic Bloch–Grüneisen (equation (1)) models. Panel (a) shows data collected on $TiNiCu_{0.025}Sn$ with Cu interstitials, which agrees well with APS up to around 700 K. Panel (b) is a similar chemical system, digitised from [18, 19], but has better agreement with the Bloch–Grüneisen model. Panel (c) shows measured data for $V_{1-\delta}CoSb$ and $Nb_{1-\delta}CoSb$, which are in good agreement with metallic Bloch–Grüneisen behaviour. Panel (d) shows data on $Nb_{0.8}Ti_{0.2}FeSb$ (digitised from [27]), which again shows APS above 300 K but deviates below room temperature.

independently of the doping. All datasets were fitted to either the APS or AS model allowing for intrinsic carrier excitations where needed (equation (3) or (4)). All fit parameters are summarised in tables 1 and 2.

Figure 4(a) shows the $Ti_{1-x}Ta_xNi_{0.92}Sn$ series [30], which immediately illustrates the complication of intrinsic behaviour in $\rho(T)$. The most highly doped samples ($x = 0.025$, 0.03 and 0.05) agree well with an APS temperature dependence. The $x = 0.01$ sample has a weak temperature dependence and shows a crossover to semiconducting behaviour due to intrinsic carrier excitations. The fits reveal a gradual decrease in ρ_0/B consistent with increasing n_H. Figure 4(b) confirms the dominance of APS for TiNiSn based materials, with $TiNiSn_{1-x}Sb_x$ showing a significant ρ_0 contribution and a moderate temperature dependence [31].

The heavily alloyed $Zr_{0.35}Hf_{0.65}Ni_{1-z}Pt_zSn_{0.98}Sb_{0.02}$ system in figure 4(c) is less clear cut [12]. The data lie below the AS curve, which can be achieved when ρ_0 is added to either APS or AS models. The blue fit curve assumes an AS model (equation (4)) and the fit results are given in table 2. Furthermore, this system shows some evidence of intrinsic carrier contributions, making the behaviour much harder to untangle. Table 2 also shows the results of trial fits to the APS model (equation (3)), which can also describe the data. However, given the presence of alloying on all three atomic sites, the dominance of AS is not unreasonable. Collection of data below 300 K is needed to make an unambiguous assignment of the dominant scattering mechanism. The fitted ρ_0 increases with Pt/Ni alloying (table 2), suggesting that the impact of alloying is partially incorporated in the temperature independent term.

The $V_{0.955-y}Ti_yCoSb$ [32] and $Nb_{1-x}CoSb$ [24] systems are shown in figures 4(d) and (e). The V system is consistent with APS with a significant ρ_0 contribution and a strong intrinsic contribution above 700 K. In the Nb system, the dependence on intrinsic carriers is apparent, with a stronger intrinsic contribution in less highly doped samples. The strong temperature dependence in each sample confirms that both are dominated by APS. Like the data presented in figure 3(c), the temperature dependence is more consistent with a metallic Bloch–Grüneisen temperature dependence.

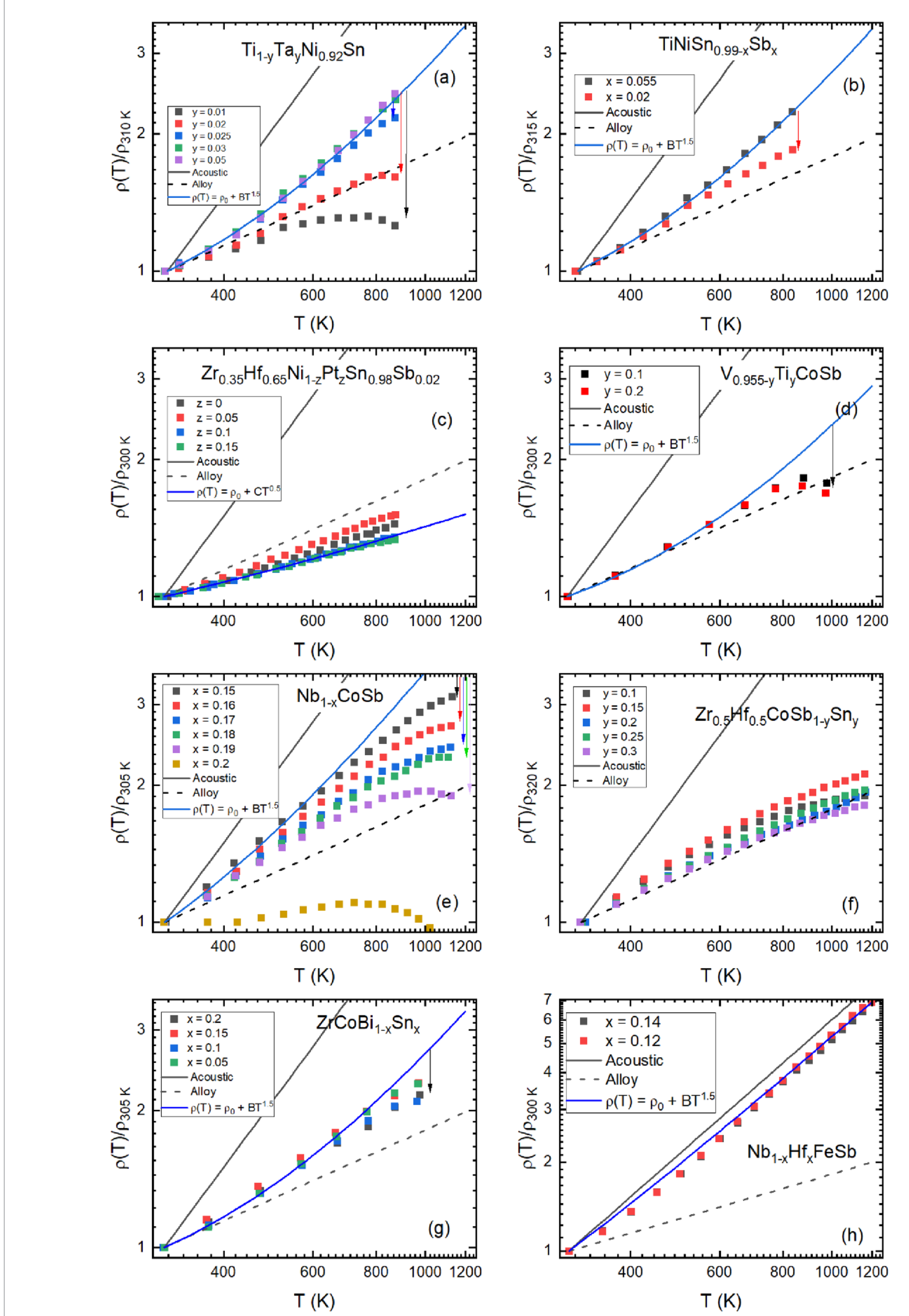

Figure 4. Log–log plot of 300 K normalized electrical resistivities ($\rho(T)/\rho_{300\,\mathrm{K}}$) for a range of HH systems. Solid black lines denote perfect $T^{1.5}$ APS behaviour; dashed black line denote perfect $T^{0.5}$ AS behaviour. Arrows indicate decreases in $\rho(T)$ due to intrinsic carrier excitations. Blue lines are fits to the data with the fitting model indicated in each panel. Fit parameters and references are given in tables 1 and 2.

The $Zr_{0.5}Hf_{0.5}CoSb_{1-y}Sn_y$ system (figure 4(f)) is another likely example of AS dominance [33]. These samples lie slightly above the AS line, suggesting that they are dominated by AS with a small ρ_0. Alternatively, the data could be interpreted as APS with a substantial ρ_0 over a wide temperature range. This is another case where low temperature data is needed to clarify the precise scattering mechanism.

The $ZrCoBi_{1-x}Sn_x$ system is shown in figure 4(g) [34]. At first glance all samples are in good agreement with equation (3), suggesting semiconducting APS and intrinsic carrier excitations. However, due to the large

Table 2. Comparison of fit parameters for the APS and AS models fitted to resistivity data on $Zr_{0.35}Hf_{0.65}Ni_{1-z}Pt_zSn_{0.98}Sb_{0.02}$ shown in figure 4(c). Original data from [12].

	APS (equation (3))				AS (equation (4))	
z	ρ_0 ($\mu\Omega$ m)	B ($\times10^{-4}$ $\mu\Omega$ m $K^{-1.5}$)	A ($\mu\Omega$ m)	E_g (eV)	ρ_0 ($\mu\Omega$ m)	C ($\mu\Omega$ m $K^{-0.5}$)
0	3.69	1.25	0.44	0.5	1.46	0.162
0.05	4.21	1.78	0.44	0.5	1.20	0.223
0.10	5.34	1.55	0.38	0.5	2.98	0.183
0.15	7.52	2.11	0.28	0.5	4.38	0.243

intrinsic contribution, there is no temperature range where a large upturn in $\rho(T)$ exists that would explicitly support a $T^{1.5}$ temperature dependence, as opposed to a T^1 dependence. This is another system where low temperature data is needed to clarify the carrier scattering mechanism and confirm ρ_0, which points to an increase in residual disorder with Bi/Sn alloying, similar to the $Zr_{0.35}Hf_{0.65}Ni_{1-z}Pt_zSn_{0.98}Sb_{0.02}$ system.

The $Nb_{1-x}Hf_xFeSb$ samples shown in figure 4(h) [28], match well with the APS model (equation (2)) with a small ρ_0 contribution (table 1). This is similar to the $Nb_{0.8}Ti_{0.2}FeSb$ sample presented in figure 3.

To summarise, the $X_{V0.8}CoSb$ materials display metallic APS behaviour (T^1), the X_VFeSb system consistently behaves as regular semiconductor ($T^{1.5}$). The $X_{IV}NiSn$ family has been found to show dominant Bloch–Grüneisen, APS and AS scattering. There is a stark contrast in temperature dependence between the X_VFeSb and $X_{IV}NiSn$ systems: the latter have small B and relatively large ρ_0, whilst the former materials have large B compared to ρ_0.

In the following section, B will be defined in terms of an effective deformation potential (E_{def}), which quantifies the strength of electron–phonon scattering.

5. Evaluation of deformation potential from the *B* parameter

The deformation potential (E_{def}) characterises the strength of the coupling between acoustic phonons and electronic charge carriers. This can be evaluated from the temperature dependence of the mobility, μ [13, 35]:

$$\mu = \frac{8\pi^{\frac{1}{2}} e\hbar^4 v_l^2 \rho_d}{3E_{def}^2 m_b^{*\frac{5}{2}} (k_B T)^{\frac{3}{2}}} \tag{5}$$

here, ${v_l}^2\rho_d$ is an approximation for the elastic constant [12], where v_l is the longitudinal sound velocity, ρ_d is the crystal density, and ${m_b}^*$ is the band effective mass of the charge carriers. This expression has the same temperature dependence as the APS model (equation (2)). After subtraction of the disorder contribution (ρ_0), leaving the temperature dependent term ($BT^{1.5}$) this yields:

$$1/ = n_H e \mu_H = \frac{1}{BT^{\frac{3}{2}}} \tag{6}$$

and from substitution and rearrangement in equation (5):

$$E_{def} = \left[\frac{8\pi^{\frac{1}{2}} e^2 \hbar^4}{3k_B^{\frac{3}{2}}} \frac{B n_H v_l^2 \rho_d}{m_b^{*\frac{5}{2}}}\right]^{0.5}. \tag{7}$$

This equation is reasonable with larger E_{def} being correlated to larger B and hence stronger APS. As noted previously [12], μ_H decreases with n_H, which if uncorrected would lead to a large n_H dependence of E_{def}. To account for this, the following correction valid at 300 K is applied [36]:

$$\mu_H = \mu_0 \left[1 + \left(\frac{n_H}{2D\left(\frac{m_{DoS}^*}{m_e}\right)^{\frac{3}{2}}}\right)\right]^{-\frac{1}{3}} \tag{8}$$

where $D = 1.5 \times 10^{20}$ cm^{-3} is a constant, which slightly differs from the original methodology [36] due to the difference between chemical carrier concentration n and Hall concentration n_H. ${m^*}_{DoS}$ is the density of states effective mass and μ_0 is the mobility in the limit of $n_H \to 0$.

For cases where a $T^{1.5}$ dependence describes $\rho(T)$, E_{def} can then be determined. The calculated values are summarised in table 1. This shows that ZrNiSn based materials have $E_{def} \sim$ 5–8 eV, TiNiSn materials have

slightly higher $E_{def} \sim$ 7–9 eV, $ZrCoBi_{1-x}Sn_x$ has $E_{def} \sim$ 7.5–9 eV, TaFeSb based materials have $E_{def} \sim$ 10 eV and NbFeSb based materials have $E_{def} \sim$ 12–14 eV. These values are in good agreement with literature values obtained using single parabolic band analysis [4, 10, 12, 21].

As is clear from the values given, even with the n_H correction, a range of E_{def} values are found. In case of lightly doped samples, this may be linked to an underestimation of B due to the difficulty of disentangling degenerate from intrinsic contributions. This may occur in $Ti_{1-x}Ta_xNi_{0.92}Sn$, where E_{def} increases from 7.1 to 8.9 eV. A similar trend is seen in the $ZrCoBi_{1-x}Sn_x$ series. However, there are other systems where this cause can be excluded. For example in both single crystal and polycrystalline $ZrNiSn_{1-x}Sb_x$, E_{def} increases from 6.8 to 7.9 eV, despite the absence of intrinsic carrier effects. This suggests that the introduction of even small amounts of Sb has a substantial impact on the coupling with acoustic phonons.

6. Discussion

Fitting $\rho(T)$ provides a straightforward way to obtain insight into the carrier scattering mechanism of HH thermoelectrics. The common approach of plotting logarithmic axes and straight-line fitting is not appropriate due to the presence of large ρ_0 contributions in HH materials. This leads to a weaker apparent temperature dependence, potentially leading to misassignment of the dominant carrier scattering mechanism. An alternative approach is proposed for systems where only high-temperature data is available. This uses $\rho(T)$ normalised with respect to ρ_X at temperature X. Combined with fitting $\rho(T)$ this provides a promising way to establish the dominant carrier scattering mechanism, although in all cases low-temperature data is needed to reach unambiguous conclusions. Fitting of a range of $\rho(T)$ data covering the main HH families shows that APS is the dominant scattering mechanism with not many clear examples of AS based on the temperature dependence of $\rho(T)$. Both semiconducting ($\sim T^{1.5}$) and metallic ($\sim T^1$) APS temperature dependences are observed, without a clear link to n_H, as might have been expected from the basic scattering models [14, 15]. In all cases a substantial temperature independent ρ_0 term is found. This signals the presence of substantial disorder in the HH materials. The precise origin of this disorder is not known but the HH literature shows the existence of a wide range of point defects (e.g. interstitials, vacancies, carrier dopants and alloying) and various forms of phase segregation [1]. The presence of a large ρ_0 is not unexpected for highly doped samples, because the common non-APS mechanisms, including IIS and AS are predicted to become temperature independent in the degenerate limit [14, 15]. This means that all non-APS is captured by ρ_0, as it is in the Bloch–Grüneisen model. We observe a similar situation for samples that have semiconductor APS. In most cases AS scattering appears to be incorporated in ρ_0, and does not give rise to a different temperature dependence, as predicted in the non-degenerate limit [14, 15]. Nevertheless, there are some systems that do show an AS ($\sim T^{0.5}$) temperature dependence. However, even in these cases a significant ρ_0 is found. The data therefore suggests that AS can manifest both in ρ_0 and in the temperature dependence. The most unambiguous confirmation of AS is to establish a $x(1-x)$ composition dependence, which would enable separation from other disorder effects that contribute to ρ_0. Further investigations aimed at disentangling possible contributions to ρ_0 are of considerable interest.

Figure 5 gives an overview of the relative strength of residual disorder and temperature dependent scattering ($\rho_0/B - n_H$) for the HH families that have dominant semiconductor APS. This shows that the X_VFeSb materials consistently have lower ρ_0/B, which is largely due to a large B. For all other families, ρ_0/B is higher and spans a relatively narrow range (8–20 $\times$ 10^3 $K^{1.5}$ covers most samples) reflecting larger inherent structural disorder and weaker coupling with acoustic phonons. In the $X_{IV}NiSn$ system, the large ρ_0 could be linked to the interstitial Ni defect, which has been shown to reduce μ and cause reduced lattice thermal conductivities [26]. Minimising interstitial Ni to levels observed in the X_VFeSb family (X_V = Nb, Ta; < 1% Fe) [29] is likely to significantly increase the electronic performance. The temperature dependence of $\rho(T)$ in the $X_{IV}NiSn$ and X_VFeSb families is fundamentally different due to the larger E_{def} in the X_VFeSb materials, up to 14 eV, where n-type ZrNiSn based compositions have E_{def} as low as 5 eV, leading to a weak temperature dependence in the latter. The other materials systems investigated have intermediate E_{def} values.

To conclude, the temperature dependence of the electrical resistivity for all the major HH families has been analysed using a modified approach that explicitly considers a temperature independent residual resistivity. This suggests that most HH materials have APS limited electronic transport but often accompanied by large temperature independent contributions due to structural disorder.

7. Methods

Data from the literature was digitised using the Engauge Digitizer software [37]. Source references are acknowledged in tables 1 and 2, and throughout the manuscript text.

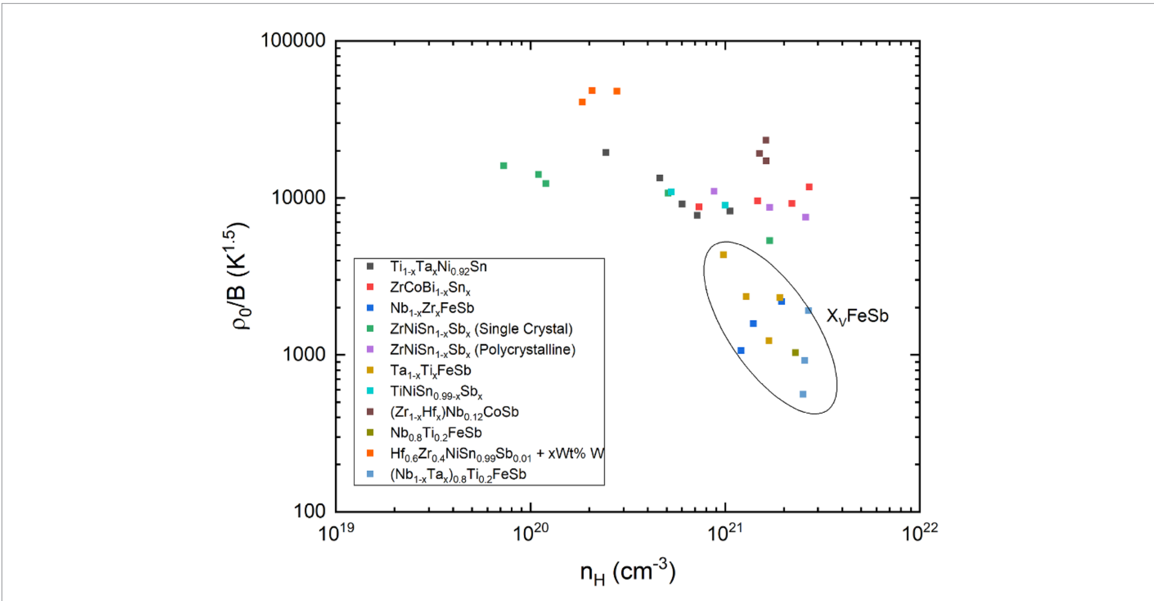

Figure 5. A plot of ρ_0/B against carrier concentration n_H for a range of HH systems that have dominant semiconductor APS. The X_VFeSb samples have low ρ_0 and relatively large B values, leading to a clear separation from the other HH families. The fitted values for ρ_0 and B and source references are given in table 1.

Original data on $TiNiCu_{0.025}Sn$, $V_{1-\delta}CoSb$ and $Nb_{1-\delta}CoSb$ samples are shown in figure 3. The synthesis and high-temperature properties of the $X_{V1-\delta}CoSb$ samples was reported previously [25]. The $TiNiCu_{0.025}Sn$ sample was prepared by arc-melting elemental pieces of Ti, Ni, Sn and Cu (all Alfa Aesar, >99.9%). Approximately 3 g of material was arc-melted in a MAM-1 arc-melting furnace under Ar atmosphere with Zr getter, flipped over and melted again. A bar was cut from the ingot using a diamond saw and annealed in an evacuated silica ampoule (with the bar wrapped in Ta foil) at 900 °C for 7 d. The basic structural and thermoelectric properties of the $TiNiCu_ySn$ series prepared using a powder route can be found in [38, 39]. The high temperature electrical resistivity of the three samples were measured using a Linseis LSR-3 apparatus. Low temperature data were collected using Quantum Design PPMS-9 apparatus.

Data availability statement

All data that support the findings of this study are included within the article (and any supplementary files).

Acknowledgments

The EPSRC (EP/N01717X/1) and Leverhulme Trust (RPG-2020-177) are acknowledged for funding. The STFC is acknowledged for access to the Materials Characterisation Laboratory at the Rutherford Appleton Laboratory.

Conflict of interest

There are no conflicts of interest to declare.

Author credit statement

R J Q and J W G B designed the study and wrote the paper. R J Q undertook the data analysis. G B G S assisted wih low-temperature resistivity data collection.

ORCID iDs

Robert J Quinn https://orcid.org/0000-0003-3146-8848
Jan-Willem G Bos https://orcid.org/0000-0003-3947-2024

References

[1] Bos J W G 2021 *Thermoelectric Energy Conversion* ed R Funahashi (Cambridge: Woodhead Publishing) pp 125–42
[2] Quinn R J and Bos J W G 2021 *Mater. Adv.* **2** 6246
[3] Poon S J 2019 *J. Phys. D: Appl. Phys.* **52** 493001
[4] Zhu T, Fu C, Xie H, Liu Y and Zhao X 2015 *Adv. Energy Mater.* **5** 1500588
[5] Bos J W G and Downie R A 2014 *J. Phys.: Condens. Matter* **26** 433201
[6] Chen S and Ren Z 2013 *Mater. Today* **16** 387–95
[7] Liu Y, Xie H, Fu C, Snyder G J, Zhao X and Zhu T 2015 *J. Mater. Chem.* A **3** 22716–22
[8] Liu Y, Fu C, Xia K, Yu J, Zhao X, Pan H, Felser C and Zhu T 2018 *Adv. Mater.* **30** 1800881
[9] Graziosi P, Kumarasinghe C and Neophytou N 2019 *J. Appl. Phys.* **126** 155701
[10] Barczak S A *et al* 2019 *J. Mater. Chem.* A **7** 27124–34
[11] Ren Q *et al* 2020 *Nat. Commun.* **11** 3142
[12] Xie H, Wang H, Pei Y, Fu C, Liu X, Snyder G J, Zhao X and Zhu T 2013 *Adv. Funct. Mater.* **23** 5123–30
[13] Bardeen J and Shockley W 1950 *Phys. Rev.* **80** 72–80
[14] Vining C B 1991 *J. Appl. Phys.* **69** 331–41
[15] Lundstrom M 2000 *Fundamentals of Carrier Transport* 2nd edn (Cambridge: Cambridge University Press)
[16] Ziman J M 2001 *Electrons and Phonons: The Theory of Transport Phenomena in Solids* (Oxford: Oxford University Press)
[17] Wang H, Gurunathan R, Fu C, Cui R, Zhu T and Snyder G J 2022 *Mater. Adv.* **3** 734–55
[18] Rogl G, Sauerschnig P, Rykavets Z, Romaka V V, Heinrich P, Hinterleitner B, Grytsiv A, Bauer E and Rogl P 2017 *Acta Mater.* **131** 336–48
[19] Rogl G, Yubuta K, Romaka V V, Michor H, Schafler E, Grytsiv A, Bauer E and Rogl P 2019 *Acta Mater.* **166** 466–83
[20] Qiu Q, Liu Y, Xia K, Fang T, Yu J, Zhao X and Zhu T 2019 *Adv. Energy Mater.* **9** 1803447
[21] He R *et al* 2016 *Proc. Natl Acad. Sci. USA* **113** 13576–81
[22] Kuo J J, Kang S D, Imasato K, Tamaki H, Ohno S, Kanno T and Snyder G J 2018 *Energy Environ. Sci.* **11** 429–34
[23] Harrison J W and Hauser J R 1976 *Phys. Rev.* B **13** 5347–50
[24] Xia K, Liu Y, Anand S, Snyder G J, Xin J, Yu J, Zhao X and Zhu T 2018 *Adv. Funct. Mater.* **28** 1705845
[25] Ferluccio D A, Halpin J E, Macintosh K L, Quinn R J, Don E, Smith R I, Maclaren D A and Bos J W G 2019 *J. Mater. Chem.* C **7** 6539–47
[26] Barczak S A, Buckman J, Smith R I, Baker A R, Don E, Forbes I and Bos J W G 2018 *Materials* **11** 536
[27] Pang H-J, Fu C-G, Yu H, Chen L-C, Zhu T-J and Chen X-J 2018 *J. Appl. Phys.* **123** 235106
[28] Fu C, Bai S, Liu Y, Tang Y, Chen L, Zhao X and Zhu T 2015 *Nat. Commun.* **6** 8144
[29] Ferluccio D A, Kennedy B F, Barczak S A, Popuri S R, Murray C, Pollet M and Bos J W G 2021 *J. Phys. Energy* **3** 035001
[30] Ren W, Zhu H, Mao J, You L, Song S, Tong T, Bao J, Luo J, Wang Z and Ren Z 2019 *Adv. Electron. Mater.* **5** 1900166
[31] Tang Y, Li X, Martin L H J, Cuervo Reyes E, Ivas T, Leinenbach C, Anand S, Peters M, Snyder G J and Battaglia C 2018 *Energy Environ. Sci.* **11** 311–20
[32] Li S *et al* 2020 *Ann. Phys.* **532** 1900440
[33] Hu C, Xia K, Chen X, Zhao X and Zhu T 2018 *Mater. Today Phys.* **7** 69–76
[34] Zhu H *et al* 2018 *Nat. Commun.* **9** 2497
[35] Shuai Z, Wang L and Song C 2012 *Theory of Charge Transport in Carbon Electronic Materials* (Berlin: Springer) pp 67–88
[36] Zhu J, Zhang X, Guo M, Li J, Hu J, Cai S, Cai W, Zhang Y and Sui J 2021 *npj Comput. Mater.* **7** 116
[37] Mitchell M 2020 Engauge digitizer (https://doi.org/10.5281/zenodo.3941227)
[38] Barczak S A, Halpin J E, Buckman J, Decourt R, Pollet M, Smith R I, MacLaren D A and Bos J W G 2018 *ACS Appl. Mater. Interfaces* **10** 4786–93
[39] Downie R A, Smith R I, MacLaren D A and Bos J W G 2015 *Chem. Mater.* **27** 2449–59
[40] Zhu H, Mao J, Feng Z, Sun J, Zhu Q, Liu Z, Singh D J, Wang Y and Ren Z 2019 *Sci. Adv.* **5** eaav5813
[41] Zhu H *et al* 2019 *Nat. Commun.* **10** 270
[42] Yu J, Fu C, Liu Y, Xia K, Aydemir U, Chasapis T C, Snyder G J, Zhao X and Zhu T 2018 *Adv. Energy Mater.* **8** 1701313
[43] Kang H B, Poudel B, Li W, Lee H, Saparamadu U, Nozariasbmarz A, Kang M G, Gupta A, Heremans J J and Priya S 2020 *Mater. Today* **36** 63–72